# Application of relativistic mean field and effective field theory densities to scattering observables for Ca isotopes

M. Bhuyan,[1,2] R. N. Panda,[3] T. R. Routray,[2] and S. K. Patra[1]
[1]*Institute of Physics, Sachivalaya Marg, Bhubaneswar-751 005, India*
[2]*School of Physics, Sambalpur University, Jyotivihar, Burla 768 019, India*
[3]*Department of Physics, ITER, Siksha O Anusandhan University, Bhubaneswar-751 030, India*
(Received 29 June 2010; revised manuscript received 13 October 2010; published 9 December 2010)

In the framework of relativistic mean field (RMF) theory, we have calculated the density distribution of protons and neutrons for $^{40,42,44,48}$Ca with NL3 and G2 parameter sets. The microscopic proton-nucleus optical potentials for $p + {}^{40,42,44,48}$Ca systems are evaluated from the Dirac nucleon-nucleon scattering amplitude and the density of the target nucleus using relativistic-Love-Franey and McNeil-Ray-Wallace parametrizations. We have estimated the scattering observables, such as the elastic differential scattering cross section, analyzing power and the spin observables with the relativistic impulse approximation (RIA). The results have been compared with the experimental data for a few selective cases and we find that the use of density as well as the scattering matrix parametrizations are crucial for the theoretical prediction.

DOI: 10.1103/PhysRevC.82.064602 PACS number(s): 25.60.Bx, 25.10.+s, 26.60.Gj, 26.30.Ef

## I. INTRODUCTION

The study of nuclear reactions is a challenging subject of nuclear physics both in theory and in the laboratory. This is useful to explain the nuclear structure of stable as well as exotic nuclei. The nucleon-nucleus interaction provides a wide source of information to determine the nuclear structure including spin, isospin, momenta, and densities, and gives a clear path toward the formation of exotic nuclei in the laboratory. In this context the study of elastic scattering of the nucleon-nucleus interaction is more interesting than that of the nucleus-nucleus interaction at different energies. One of the theoretical methods to study this type of reaction is the relativistic impulse approximation (RIA). It is a microscopic theory where the Dirac optical potential is constructed from the Lorentz invariant nucleon-nucleon (NN) amplitudes obtained from relativistic meson exchange models. The basic ingredients in this approach are the NN scattering amplitude and the nuclear scalar and vector densities [1] of the target nucleus. This approach can be extended to elastic scattering of composite particles [2]. In this context proton-nucleus ($p$-$A$) elastic scattering is of particular interest because of its relative simplicity with which it provides a satisfactory description of the reaction dynamics.

One useful application of RIA is to generate a microscopic optical potential to study the elastic and inelastic scattering of nucleons for unstable proton- and/or neutron-rich nuclei. The RIA folding procedure can also be extended to calculate microscopic optical potentials for exotic nuclei using the relativistic mean field formalism [3,4].

The first theoretical introduction to elastic scattering was given by Chew [5] almost six decades ago. For a wide range of energy intervals, impulse approximation (IA) produces the main qualitative description on quasielastic scattering for $A \leqslant 64$ nuclei [6]. During the same time, Glauber [7] studied the reaction dynamics of the composite system at low energies, but one cannot predict the extension of quasielastic scattering using this model. Further, the generalized Glauber formula and the unitarized impulse approximation [8,9] were circumvented. But the development of RIA opens a path to study the above-mentioned scattering phenomenon for both the elastic and the quasielastic particles. This field of research was further strengthened by the experimental evidences of cross-section and analyzing power for the scattering systems $\vec{p} + {}^{12}$C, $p + {}^{9}$B, and $p + {}^{16}$O at 200 MeV, which were measured over a wide range of momentum transfer $>6$ fm$^{-1}$ at IUCF [10,11]. Recent studies of proton nucleus elastic scattering within the modified (Coulomb) Glauber model [12,13] and the global Dirac optical potential [14] have motivated us to study the elastic scattering phenomenon. For convenience, we consider Ca isotopes as targets and $p$ as a projectiles, because Ca satisfies the relativistic mean field nuclear structure model accurately without recoil correction to the Dirac scattering equation.

In the present paper, our aim is to calculate the nucleon-nucleus elastic differential scattering cross section ($\frac{d\sigma}{d\Omega}$) and other related physical quantities such as optical potential ($U_{\rm opt}$), analyzing power ($A_y$), and spin rotation parameter ($Q$ value) using relativistic mean field (RMF) and the recently proposed effective field theory motivated relativistic mean field (ERMF) densities. These are obtained from the successful NL3 [15] and the advanced G2 [16] parameter sets, which are given in Sec. II. In Secs. III and IV, the details of target densities folded with the NN amplitude for various energetic proton projectiles with the relativistic-Love-Franey (RLF) [17,18] and McNeil-Ray-Wallace (MRW) parametrizations [19] for $^{40,42,44,48}$Ca are given. In these sections we have outlined the expressions for the differential elastic scattering cross section, analyzing power, and spin observables. Section V describes the results obtained from our calculations. Finally, a brief summary and conclusions are given in Sec. VI for the present work.

## II. RMF AND ERMF FORMALISMS

A documentation of RMF and ERMF formalisms are available in Refs. [20] and [16,21], respectively, for both finite and infinite nuclear matter. Here only the energy density functional and associated expressions for the densities are

 

presented [22,23]:

$$\mathcal{E}(\mathbf{r}) = \sum_{\alpha} \varphi_{\alpha}^{\dagger} \Big\{ -i\boldsymbol{\alpha}\cdot\boldsymbol{\nabla} + \beta(M-\Phi) + W + \frac{1}{2}\tau_3 R + \frac{1+\tau_3}{2}A - \frac{i}{2M}\beta\boldsymbol{\alpha}\cdot\Big(f_v\boldsymbol{\nabla}W + \frac{1}{2}f_\rho\tau_3\boldsymbol{\nabla}R + \lambda\boldsymbol{\nabla}A\Big) + \frac{1}{2M^2}(\beta_s + \beta_v\tau_3)\,\Delta A \Big\}\varphi_{\alpha} + \Big(\frac{1}{2} + \frac{\kappa_3}{3!}\frac{\Phi}{M} + \frac{\kappa_4}{4!}\frac{\Phi^2}{M^2}\Big)\frac{m_s^2}{g_s^2}\Phi^2 - \frac{\zeta_0}{4!}\frac{1}{g_v^2}W^4 + \frac{1}{2g_s^2}\Big(1+\alpha_1\frac{\Phi}{M}\Big)(\boldsymbol{\nabla}\Phi)^2 - \frac{1}{2g_v^2}\Big(1+\alpha_2\frac{\Phi}{M}\Big)(\boldsymbol{\nabla}W)^2 - \frac{1}{2}\Big(1+\eta_1\frac{\Phi}{M} + \frac{\eta_2}{2}\frac{\Phi^2}{M^2}\Big)\frac{m_v{}^2}{g_v{}^2}W^2 - \frac{1}{2g_\rho^2}(\boldsymbol{\nabla}R)^2 - \frac{1}{2}\Big(1+\eta_\rho\frac{\Phi}{M}\Big)\frac{m_\rho^2}{g_\rho^2}R^2 - \frac{1}{2e^2}(\boldsymbol{\nabla}A)^2 + \frac{1}{3g_\gamma g_v}A\Delta W + \frac{1}{g_\gamma g_\rho}A\Delta R, \tag{1}$$

where the index $\alpha$ runs over all occupied states $\varphi_\alpha(\mathbf{r})$ of the positive energy spectrum, $\Phi \equiv g_s\phi_0(\mathbf{r})$, $W \equiv g_v V_0(\mathbf{r})$, $R \equiv g_\rho b_0(\mathbf{r})$, and $A \equiv eA_0(\mathbf{r})$.

The terms with $g_\gamma$, $\lambda$, $\beta_s$, and $\beta_v$ take care of the effects related with the electromagnetic structure of the pion and the nucleon (see Ref. [23]). Specifically, the constant $g_\gamma$ concerns the coupling of the photon to the pions and the nucleons through the exchange of neutral vector mesons. The experimental value is $g_\gamma^2/4\pi = 2.0$. The constant $\lambda$ is needed to reproduce the magnetic moments of the nucleons, defined by

$$\lambda = \tfrac{1}{2}\lambda_p(1+\tau_3) + \tfrac{1}{2}\lambda_n(1-\tau_3), \tag{2}$$

with $\lambda_p = 1.793$ and $\lambda_n = -1.913$ being the anomalous magnetic moments of the proton and the neutron, respectively. The terms with $\beta_s$ and $\beta_v$ contribute to the charge radii of the nucleon [23].

The energy density contains tensor couplings, scalar-vector, and vector-vector meson interactions in addition to the standard scalar self-interactions $\kappa_3$ and $\kappa_4$. Thus the ERMF formalism can be interpreted as a covariant formulation of density functional theory as it contains all the higher order terms in the Lagrangian, obtained by expanding it in powers of the meson fields. The terms in the Lagrangian are kept finite by adjusting the parameters. Further insight into the concepts of the ERMF model can be obtained from Ref. [23]. It may be noted that the standard RMF Lagrangian is obtained from that of the ERMF by ignoring the vector-vector and scalar-vector cross interactions, and hence does not need a separate discussion.

In each of the two formalisms (ERMF and RMF), the set of coupled equations are solved numerically by a self-consistent iteration method. The baryon, scalar, isovector, proton, and tensor densities are

$$\rho(r) = \sum_{\alpha} \varphi_{\alpha}^{\dagger}(r)\varphi_{\alpha}(r), \tag{3}$$

$$\rho_s(r) = \sum_{\alpha} \varphi_{\alpha}^{\dagger}(r)\beta\varphi_{\alpha}(r), \tag{4}$$

$$\rho_3(r) = \sum_{\alpha} \varphi_{\alpha}^{\dagger}(r)\tau_3\varphi_{\alpha}(r), \tag{5}$$

$$\rho_p(r) = \sum_{\alpha} \varphi_{\alpha}^{\dagger}(r)\left(\frac{1+\tau_3}{2}\right)\varphi_{\alpha}(r), \tag{6}$$

$$\rho_T(r) = \sum_{\alpha} \frac{i}{M}\boldsymbol{\nabla}\cdot[\varphi_{\alpha}^{\dagger}(r)\beta\boldsymbol{\alpha}\varphi_{\alpha}(r)], \tag{7}$$

$$\rho_{T,3}(r) = \sum_{\alpha} \frac{i}{M}\boldsymbol{\nabla}\cdot[\varphi_{\alpha}^{\dagger}(r)\beta\boldsymbol{\alpha}\tau_3\varphi_{\alpha}(r)]. \tag{8}$$

These densities are obtained from the RMF and ERMF formalisms with NL3 [15] and G2 [16] parametrizations. We refer the readers to Refs. [20,21] for numerical details and ground state equations for finite nuclei.

## III. THE NUCLEON-NUCLEON SCATTERING AMPLITUDE

The nonlinear relativistic impulse approximation (RIA) involves mainly two steps [24–26] of calculation. Basically a particular set of Lorentz covariant functions [19], which multiply with the so-called Fermi invariant Dirac matrix, represent the nucleon-nucleon (NN)-scattering amplitudes. These functions are then folded with the target densities of protons and neutrons from the relativistic Langragian for the NL3 and G2 parameter sets to produce a first-order complex optical potential. The invariant NN-scattering operator $\mathcal{F}$ can be written in terms of five complex functions (the five terms involved in the proton-proton $pp$ and neutron-neutron $nn$ scattering). In general RIA, the function $\mathcal{F}$ can be expressed as [24–26]

$$\mathcal{F}(q,E) = \sum_{L=S}^{\mathrm{PS}} \mathcal{F}^L(q,E)\lambda_{(0)}^L \cdot \lambda_{(1)}^L, \tag{9}$$

where $\lambda^L$ stands for the Dirac operator and (0) and (1) stand for the incident and struck nucleons, respectively. $S$, $V$, $T$, $A$, and PS stand for scalar, vector, axial vector, tensor, and pseudoscalar. The dot product $(\cdot)$ implies that all Lorentz indices are contracted. The Dirac spinor is defined as the initial and final two nucleons by taking the matrix elements of $\mathcal{F}$, which represent the NN-scattering amplitudes. The functions $\mathcal{F}^L$ are determined by equating the resultant amplitude (in the center-of-mass frame) to the empirical amplitude, which is conventionally expressed in term of the nonrelativistic Wolfenstein amplitudes $A_1, A_2, \ldots A_5$ [19]. Since there are five complex invariant amplitudes and $A_1, A_2, \ldots A_5$ are five Wolfenstein amplitudes, the relation among them is determined by a $5 \times 5$ nonsingular matrix, whose inversion is

straightforward. However, $\mathcal{F}$ is an operator in the two-particle Dirac space and the component is canceled out due to isospin and parity invariance and we get only 44 components [27]. From this it is clear that $\mathcal{F}$ is not unique. In other words, there are an infinite number of operators $\mathcal{F}$ with same five on-shell but different negative (energy) elements. The expression of $\mathcal{F}$ cannot predict a reasonable result at the lower energy region. To avoid the limitation, the pseudoscalar $\mathcal{F}^{\rm PS}$ is replaced by the pseudovector invariant, and is expressed as

$$\mathcal{F}^{\rm PS}\gamma^5_{(0)}\gamma^5_{(1)} = -\mathcal{F}^{\rm PV}\frac{\gamma^5_{(0)}}{2M}\frac{\gamma^5_{(1)}}{2M}. \tag{10}$$

The meson-nucleon couplings are complex, with a real part $g_i^2$ and an imaginary part $\overline{g_i^2}$, which can be decomposed into two parts,

$$\begin{aligned}\langle k_0'k_1'|\ \mathcal{F}\ |k_0k_1\rangle &= \langle k_0'k_1'|\ t(E)\ |k_0k_1\rangle \\ &\quad +(-1)^T\langle k_0'k_1'|t,(E)|k_0k_1\rangle,\end{aligned} \tag{11}$$

where $t(E)$ is the lowest order meson and $T$ is the total isospin of the two-nucleon state. The calculation of the one-meson exchange from the Feynman diagram [17] is represented as

$$g_i\left(\frac{\Lambda_i^2}{q^2+\Lambda_i^2}\right)\lambda^{L_{(i)}}(\tau)^{I_i}, \tag{12}$$

with $L_{(i)}$ denoting the spin and parity of the $i^{\rm th}$ meson and $I_i = (0,\ 1)$ being the meson's isospin. Here we neglect the energy transfer $q^0$ carried by the meson for different masses and cutoff parameters in the real and imaginary parts of the amplitude in Eq. (9). The contribution of the $i^{\rm th}$ meson to the NN-scattering amplitude by taking all kinematics is given as

$$\begin{aligned}&\overline{U_{0'}}\cdot\overline{U_{1'}}\mathcal{F}_i U_0U_1 \\ &\quad\propto \frac{g_i^2}{q^2+m_i^2}\left(\frac{\Lambda_i^2}{q^2+\Lambda_i^2}\right)^2\{\tau_0\cdot\tau_1\}^{I_i}\overline{U_{0'}}\lambda^{L_i}U_0 \\ &\quad\cdot\overline{U_{1'}}\lambda^{L_i}U_1 + (-1)^T\frac{g_i^2}{Q^2+m_i^2} \\ &\quad\times\left(\frac{\Lambda_i^2}{Q^2+\Lambda_i^2}\right)^2\{\tau_0\cdot\tau_1\}^{I_i}\overline{U_{1'}}\lambda^{L_i}U_0\cdot\overline{U_{0'}}\lambda^{L_i}U_1.\end{aligned} \tag{13}$$

Here the direct and exchange momentum transfer are $q = k_0' - k_0$ and $Q = k_1' - k_1$.The first term in Eq. (13), which is already of the form of Eq. (9), can easily identify the contribution of $\mathcal{F}^L$.The second term is unlike this form, so we rewrite this as

$$\begin{aligned}&\overline{U_{0'}}\cdot\overline{U_{1'}}\mathcal{F}_i U_0U_1 \\ &\quad\propto \frac{g_i^2}{q^2+m_i^2}\left(\frac{\Lambda_i^2}{q^2+\Lambda_i^2}\right)^2\{\tau_0\cdot\tau_1\}^{I_i}\overline{U_{0'}}\lambda^{L_i}U_0\cdot\overline{U_{1'}}\lambda^{L_i}U_1 \\ &\quad+(-1)^T\sum_{L'}B_{L_i}\frac{g_i^2}{Q^2+m_i^2}\left(\frac{\Lambda_i^2}{Q^2+\Lambda_i^2}\right)^2\{\tau_0\cdot\tau_1\}^{I_i} \\ &\quad\times\overline{U_{0'}}\lambda^{L_i'}U_0\cdot\overline{U_{1'}}\lambda^{L_i'}U_1,\end{aligned} \tag{14}$$

where the transformation matrix is given as

$$B_{L,L'} = \frac{1}{8}\begin{bmatrix} 2 & 2 & 1 & -2 & 2 \\ 8 & -4 & 0 & -4 & -8 \\ 24 & 0 & -4 & 0 & 24 \\ -8 & -4 & 0 & -4 & 8 \\ 2 & -2 & 1 & 2 & 2 \end{bmatrix}. \tag{15}$$

The row and columns are labeled in the order of $S$, $V$, $T$, $A$, PS. The contribution to the Lorentz invariants ($\mathcal{F}_L$) in simpler forms are written as

$$\mathcal{F}(q,E_c) = i\frac{M^2}{2E_ck_c}\left[F_D^L(q)+F_X^L(Q)\right], \tag{16}$$

$$F_D^L(q) = \sum_i \delta_{L,L(i)}\{\tau_0\cdot\tau_1\}^{I_i}f^i(q), \tag{17}$$

$$F_X^L(Q) = (-1)^T\sum_i B_{L(i),L}\{\tau_0\cdot\tau_1\}^{I_i}f^i(Q), \tag{18}$$

$$f^i(q) \equiv \frac{g_i^2}{q^2+m_i^2}\left(\frac{\Lambda_i^2}{q^2+\Lambda_i^2}\right)^2 - i\frac{\overline{g_i^2}}{Q^2+\overline{m_i^2}}\left(\frac{\overline{\Lambda_i^2}}{q^2+\overline{\Lambda_i^2}}\right)^2. \tag{19}$$

Here $E_c$ is the total energy in the NN center-of-mass system. Note that $f^i$ depends only on the magnitude of the three-momentum transfer and the expressions are used to fit the NN-scattering amplitude at laboratory energy. The full parametrizations are framed out in Refs. [17,18].

## IV. NUCLEON-NUCLEUS OPTICAL POTENTIAL

The Dirac optical potential $U_{\rm opt}(q,\ E)$ can be written as

$$U_{\rm opt}(q,\ E) = \frac{-4\pi ip}{M}\langle\psi|\sum_{n=1}^{A}\exp\left[iq\cdot x(n)\right]\mathcal{F}(q,\ E;n)|\psi\rangle, \tag{20}$$

where $\mathcal{F}$ is the scattering operator, $p$ is the momentum of the projectiles in the nucleon-nucleus center-of-mass frame, $|\psi\rangle$ is the nuclear ground state wave function for the $A$ particle, $q$ is the momentum transfer, and $E$ is the collision energy for a stationary target (nucleus) and incident projectile (proton). In the present calculation the nuclear recoil energy is neglected because of elastic scattering. The operator $\mathcal{F}(q,\ E;n)$ describes the scattering of the projectile from target nucleon $n$ without separation into direct and exchange terms. Let us define the nuclear ground state by a Dirac-Hartree wave function [28] and the incident projectile wave function as $\mathcal{U}(x)$, then the optical potential on incident wave projected to the coordinate space can be written as

$$\begin{aligned}&\langle x|U_{\rm opt}|\mathcal{U}_0\rangle \\ &\quad= \frac{-4\pi ip}{M}\langle\psi|\sum_\alpha^{\rm occ}\int d^3y'd^3yd^3x'\mathcal{U}_\alpha(y') \\ &\qquad\times\{\langle xy'|t(E)|x'y\rangle + (-1)^T\langle y'x|t(E)|x'y\rangle\}\mathcal{U}_0(x')\mathcal{U}_\alpha(y).\end{aligned} \tag{21}$$

The antisymmetrized matrix element of $t(E)$ in coordinate space is the Fourier transform [28] of the matrix element in the momentum space coordinate and is written as

$$\begin{aligned}\langle x|U_{\rm opt}|\mathcal{U}_0\rangle &= \frac{-4\pi ip}{M}\sum_L\int d^3x'\big[\rho^L(x')t_D^L(|x-x'|;E)\big]\lambda^L\mathcal{U}_0(x)\\ &\quad-\frac{-4\pi ip}{M}\sum_L\int d^3x'\big[\rho^L(x',x)t_X^L(|x-x'|;E)\big]\lambda^L\mathcal{U}_0(x'),\end{aligned} \tag{22}$$

where

$$t_D^L(|x|;E)\equiv\int\frac{d^3q}{(2\pi)^3}t_D^L(q,E)e^{-iqx}, \tag{23}$$

with

$$t_D^L(|q|;E)\equiv\left(\frac{iM^2}{2E_ck_c}\right)F_D^L(q), \tag{24}$$

and similarly for the exchange part $t_D^L(|Q|;E)$. The nuclear density is defined by a simple expression similar to the equation of RMF and ERMF density,

$$\rho^L(x,x')\equiv\sum_\alpha^{\rm occ'}\overline{\mathcal{U}_\alpha}\lambda^L\mathcal{U}_\alpha,\ \rho^L(x)\equiv\rho^L(x',x). \tag{25}$$

The prime stands for occupied states, i.e., the sum over target protons ($pp$ amplitude) and target neutrons ($pn$ amplitude) used. The first term in Eq. (22) defines the direct optical potential,

$$U_D^L(r,E)=\frac{-4\pi ip}{M}\int d^3x'\rho^L(x')t_D^L(|x-x'|;E). \tag{26}$$

The nonlocal second term is treated in nonlocal density approximation [29], which contains plane wave status for incident and bound nucleons. We replaced the exchange integral with the local potential by

$$\begin{aligned}U_X^L(r,E)&=\frac{-4\pi ip}{M}\int d^3x'\rho^L(x',x)t_D^L(|x-x'|;E)j_0(p(|x-x'|),\end{aligned} \tag{27}$$

where $j_0$ is the spherical Bessel function. The off-diagonal one-body density is approximated by the local density, which results in

$$\rho_L(x',x)\approx\rho^L[1/2(x+x')]\left(\frac{3}{sk_f}\right)j_1(sk_f), \tag{28}$$

with $s\equiv|x-x'|$; $k_f$ is related to the nuclear baryon density by $\rho_B[1/2(x+x')]=2k_f^3/3\pi^2$. Now the optical potential has the form

$$U_{\rm opt}=U_S+\gamma^0U^V-2i\alpha\cdot\hat{r}U^T, \tag{29}$$

where

$$U^L\equiv U^L(r,E)=U_D^L(r,E)+U_X^L(r,E). \tag{30}$$

As the tensor contributions are small, by neglecting these the Dirac equation for the projectile has precisely the same form as in the RMF and ERMF equation. By taking the Fourier transform of this equation, we get the optical potential:

$$\begin{aligned}&\int\frac{d^3q}{(\pi)^3}\exp(iq\cdot x)f(q)\\ &\quad=\frac{g^2}{4\pi}\frac{\Lambda^2}{\Lambda^2-m^2}\left\{\frac{\Lambda^2}{\Lambda^2-m^2}\frac{e^{-mr}-e^{-\Lambda r}}{r}-\frac{\Lambda}{2}e^{-\Lambda r}\right\}.\end{aligned} \tag{31}$$

This equation includes all meson exchanges (except the pseudoscalar meson) with derivative coupling, which is written in the form

$$\begin{aligned}&\int\frac{d^3q}{(2\pi)^3}\exp(iq\cdot x)f(q)\frac{q^2}{4M^2}\\ &\quad=\frac{\Lambda^2}{4M^2}\frac{g^2}{4\pi}\frac{\Lambda^2}{\Lambda^2-m^2}\left\{\frac{m^2}{\Lambda^2-m^2}\frac{e^{-\Lambda r}-e^{-mr}}{r}+\frac{\Lambda}{2}e^{-\Lambda r}\right\}.\end{aligned} \tag{32}$$

The optical potential is modified by the Pauli blocking factor [30–34] $a(E)$ with local density approximation as follows:

$$U^L(r,E)\longrightarrow\left[1-a(E)\left(\frac{\rho_B(r)}{\rho_0}\right)^{2/3}\right]U^L(r,E). \tag{33}$$

Here $\rho_B$ is the local baryon density of the target and $\rho_0$ is the nuclear matter density at saturation. The approximation depends on $\rho_B^{2/3}$, which agrees with phase-space arguments based on isotropic scattering. The details about the Pauli blocking factor are given in Ref. [18]. To solve the scattering state Dirac equation, the wave function is separated into two components (upper and lower) and this equation is expressed as two coupled first-order differential equations. Elimination of the lower component leads to a single second-order differential equation with spin-orbit as well as both local and nonlocal potentials. The nonlocal Darwin potential can be separated by rewriting the upper component of the wave function, $\mathcal{A}^{1/2}(r,E)\mathcal{U}(x)$, and

$$\mathcal{A}(r,E)\equiv1+\frac{U^S(r,E)-U^V(r,E)}{E+M}. \tag{34}$$

After some algebra, the equation can be written as

$$(-\nabla^2+V_{\rm cent}+V_{\rm so}\sigma\cdot L+V_{\rm Darwin})u(x)=(E^2-M^2)u(x), \tag{35}$$

where the energy-dependent optical potentials are

$$V_{\rm cent}(r,E)=2MU^S+2EU^V+(U^S)^2-(U^V)^2, \tag{36}$$

$$V_{\rm so}(r,E)=-\frac{1}{r}\frac{B'}{B}, \tag{37}$$

$$V_{\rm Darwin}=\frac{3}{4}\left(\frac{B'}{B}\right)^2-\frac{1}{r}\frac{B'}{B}-\frac{1}{2}\frac{B''}{B}. \tag{38}$$

Since the two-component Dirac wave functions are eigenstates of $\sigma\cdot L$, by taking the second derivative of the function we can solve easily using the Numerov algorithm [35,36]. Note that $\mathcal{U}(x)$ is not equal to the upper component wave function in the region of the potential $A(r,E)\longrightarrow1$, as $r\longrightarrow\infty$ and $\mathcal{U}$ have

the same asymptotic behavior of the wave function at large $r$. Thus the correct boundary condition is imposed by matching $\mathcal{U}$ to the form of Coulomb scattering solution incident in the $z$ direction [37]:

$$\psi(r) \propto_{r\longrightarrow\infty} \left\{\exp i[pz - \eta\ln 2pr\sin^2\theta/2]\left[1 - \frac{\eta^2}{2ipr\sin^2\theta/2}\right]\right\}\chi_{\rm inc} + \left\{\frac{\exp i[pr - \eta\ln 2pr]}{r}[A(\theta) + B(\theta)\sigma\cdot\hat{n}]\right\}\chi_{\rm inc}, \quad (39)$$

with $E = \sqrt{p^2 + M^2}$. $\chi_{\rm inc}$ is a two-component Pauli spinor, $\theta$ is the scattering angle, $n$ is the normal to the scattering plane, and $\eta \equiv Ze^2/p^2$ where $Z$ is the nuclear charge. The scattering observables such as the differential scattering cross section ($\frac{d\sigma}{d\Omega}$) and other quantities, such as the optical potential ($U_{\rm opt}$), analyzing power ($A_y$), and spin observables ($Q$ value), are easily determined from the scattering amplitude, which is written as

$$\frac{d\sigma}{d\Omega} \equiv |A(\theta)|^2 + |B(\theta)|^2, \quad (40)$$

$$A_y \equiv \frac{2{\rm Re}[{\rm A}^*(\theta){\rm B}(\theta)]}{d\sigma/d\Omega}, \quad (41)$$

$$Q \equiv \frac{2{\rm Im}[{\rm A}(\theta){\rm B}^*(\theta)]}{d\sigma/d\Omega}. \quad (42)$$

## V. DETAILS OF CALCULATIONS AND RESULTS

First we calculate both the scalar and vector parts of the neutron and proton density distribution for $^{40,42,44,48}$Ca from the RMF (NL3) and ERMF (G2) formalisms [21]. Then we evaluate the scattering observables using these densities in the RIA framework [38], which involves the following two steps: (i) We generate the complex NN interaction from the Lorentz invariant matrix $\mathcal{F}^L(q, E)$ as defined in Eq. (2). Then the interaction is folded with the ground state target nuclear density for both the RLF [17,18] and MRW parameters [19] separately and obtained the nucleon-nucleus complex optical potential $U_{\rm opt}(q, E)$. It is to be noted that the pairing interaction has been taken into account using the Pauli blocking approximation. Here, the Pauli blocking enters through the intermediate states of the $t$-matrix formalism, which has geometrical effects on the optical potential. (ii) We solve the wave function of the scattering state utilizing the optical potential prepared in the first step by the well known Numerov algorithm [35]. The result is approximated with the nonrelativistic Coulomb scattering for a wide range of radial components, which yields the scattering amplitude and other observables [37]. By comparing our calculations with the available experimental data, we examine the validity of our RIA predictions for describing $\frac{d\sigma}{d\Omega}$, $A_y$, and $Q$ values, which are presented in Figs. 1–11.

### A. Neutron and proton densities

In Fig. 1, we have plotted the proton $\rho_p$ and neutron $\rho_n$ density distribution for $^{40,42,44,48}$Ca using the NL3 and G2 parameter sets within RMF and ERMF formalisms. From the figure, we note that there is a very small difference in the densities for the NL3 and G2 parameter sets. However, a careful inspection shows a small enhancement in the central density (0–1.6 fm) for the NL3 set. On the other hand, the densities obtained from G2 are elongated to a larger distance toward the tail region, and this nominal difference has a significant role to play in the scattering phenomena, which is explained later on. Further, the agreement of $\rho_p$ with the experiment [39] and $\rho_n$ with the deduced data [40] for the NL3 set is slightly better than that of G2. Explicitly, it is worth mentioning that the $\rho_p$ (NL3) matches the data even at the central region, whereas the $\rho_p$ of G2 is underestimated throughout the density plot.

A microscopic investigation of Fig. 1 shows a change in $\rho_p(r)$, $\rho_n(r)$, i.e., the area covered by the proton and neutron densities gradually increases with the mass number in an isotopic chain. From the $\rho_p(r)$ and $\rho_n(r)$, we estimate the possible relative isotopic density difference $\Delta\rho(r)$ for the RMF (NL3) and ERMF (G2) parameter sets (see Figs. 2 and 3). The calculated $\Delta\rho_p(r)$ are compared with the experimental data [41] in Fig. 2. The measured data of $\Delta\rho_p(r)$ lies in between the prediction of the NL3 and G2 values, as shown in Fig. 2. Comparing $\rho_p(^{42}{\rm Ca}) - \rho_{\rm p}(^{40}{\rm Ca})$, $\rho_p(^{44}{\rm Ca}) - \rho_{\rm p}(^{40}{\rm Ca})$, and $\rho_p(^{48}{\rm Ca}) - \rho_{\rm p}(^{40}{\rm Ca})$ of Figs. 2(a)–2(c), we notice a better agreement of NL3 values over G2 with respect to experimental

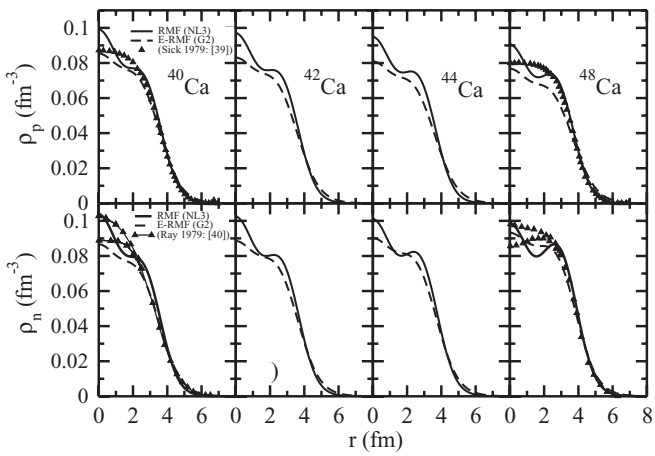


FIG. 1. The proton $\rho_p$ (upper panel) and neutron $\rho_n$ (lower panel) density distribution for $^{40,42,44,48}$Ca obtained from RMF (NL3) and ERMF (G2) parameter sets. The experimental [39] $\rho_p$ and deduced [40] $\rho_n$ for $^{40,48}$Ca are also compared.

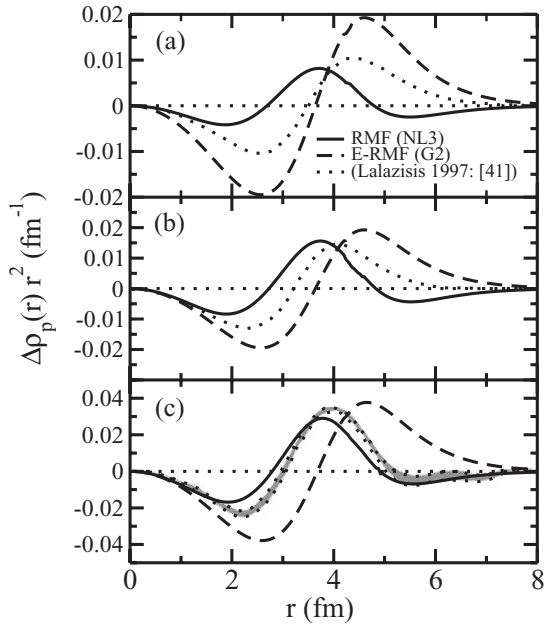


FIG. 2. The relative isotopic proton density differences $\Delta\rho_p(r)$ for $\rho_p(^{42}\mathrm{Ca}) - \rho_p(^{40}\mathrm{Ca})$, $\rho_p(^{44}\mathrm{Ca}) - \rho_p(^{40}\mathrm{Ca})$, and $\rho_p(^{48}\mathrm{Ca}) - \rho_p(^{40}\mathrm{Ca})$ obtained from RMF (NL3) and ERMF (G2) are compared with the data [41] in (a), (b), and (c), respectively.

measurement in the isotopic chain, which is subsequently reflected in the results of the scattering observables.

The relative isotopic density difference for neutron $\Delta\rho_n(r)$ is compared in Fig. 3 with the deduced neutron density difference data [42] and the density-matrix-expansion prediction [43]. The predicted results with RMF (NL3) agree well only for the double closed-shell nuclei $^{40}$Ca and $^{48}$Ca. But in the case of ERMF (G2) we get an excellent match with the deduced $\Delta\rho_n(r)$ for the considered isotopic chain. A peak appears in $\Delta\rho_n(r)$ at the radial range $r \sim 3.4$–$3.8$ fm and this peak is

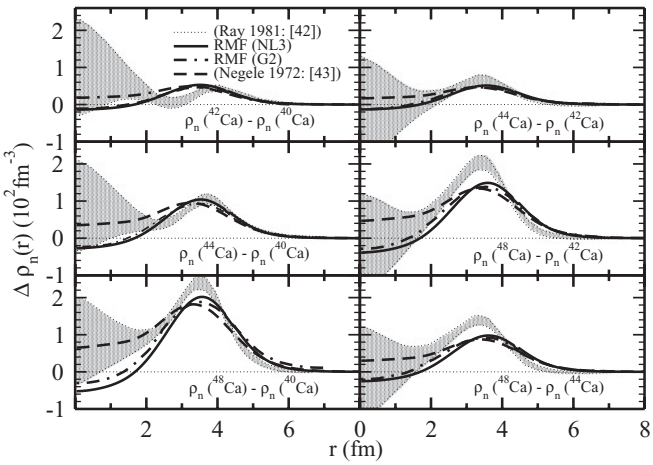


FIG. 3. The relative isotopic neutron density differences $\Delta\rho_n(r)$ for $\rho_n(^{42}\mathrm{Ca}) - \rho_n(^{40}\mathrm{Ca})$, $\rho_n(^{44}\mathrm{Ca}) - \rho_n(^{40}\mathrm{Ca})$, $\rho_n(^{48}\mathrm{Ca}) - \rho_n(^{40}\mathrm{Ca})$, $\rho_n(^{44}\mathrm{Ca}) - \rho_n(^{42}\mathrm{Ca})$, $\rho_n(^{48}\mathrm{Ca}) - \rho_n(^{42}\mathrm{Ca})$, and $\rho_n(^{48}\mathrm{Ca}) - \rho_n(^{44}\mathrm{Ca})$. The RMF (NL3) and ERMF (G2) $\Delta\rho_n(r)$ are compared with the density-matrix-expansion (DME) data [43] and the uncertainty deduced neutron difference [42].

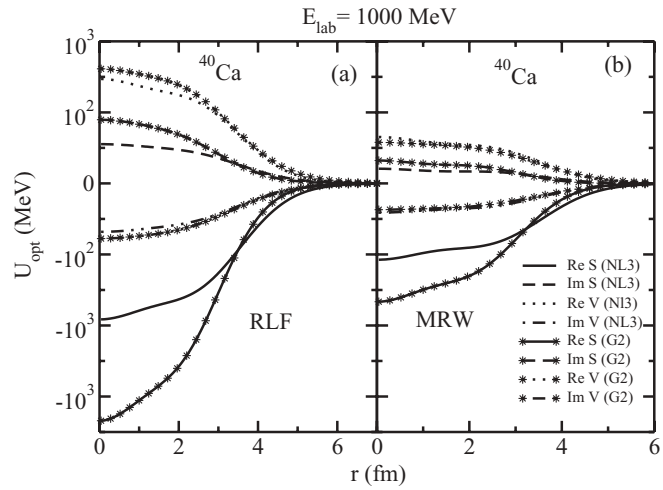


FIG. 4. The real (Re) and imaginary (Im) parts of the scalar $S$ and vector $V$ Dirac optical potential are plotted as a function of the nuclear radius for $p + ^{40}$Ca system using RMF (NL3) and ERMF (G2) densities. (a) RLF and (b) MRW parametrization. The energy of the projectile proton is $E_{\mathrm{lab}} = 1000$ MeV.

slightly shifted toward the center with the increase of neutron number. Although $\Delta\rho_n(r)$ for the G2 set gives better agreement with the deduced values, the use of the NL3 set in the RIA formalism works well for the scattering observables (shown later).

### B. Optical potential

With the densities in hand, we calculate the optical potential $U_{\mathrm{pot}}$ for $^{40,42,44,48}$Ca by folding the density matrix with the NN scattering amplitude of the proton projectile for 300, 800, and 1000 MeV. The $U_{\mathrm{pot}}$ is a complex function which constitutes both a real and an imaginary part for both the scalar and the vector potentials. In Fig. 4, we present the $U_{\mathrm{pot}}$ for $\overrightarrow{p} + ^{40}$Ca at laboratory energy $E_{\mathrm{lab}} = 1000$ MeV as a representative case. We also examine the $U_{\mathrm{pot}}$ for other Ca isotopes and find similar trends with $\overrightarrow{p} + ^{40}$Ca. In other words, we do not get any significant difference in the optical potential with the increase of neutron number. Similar to the density distribution in NL3 and G2 (Fig. 1), here we find a difference in $U_{\mathrm{opt}}(q, E)$ between the RLF and MRW parametrizations. The evaluation methods of the optical potentials using RLF or MRW (see Fig. 4) are somewhat different from each other, which are given in the Appendix [38] and are responsible for the use of the different parametrizations at various ranges of incident energies. For example, the RLF parameters used here are from Refs. [17,18] and are computed for energies up to 400 MeV and are therefore suitable for lower $E_{\mathrm{lab}}$, whereas the MRW is better for the higher values, which will be discussed in the coming sections. Further, the $U_{\mathrm{opt}}(q, E)$ values from either RLF or MRW differ significantly depending on the NL3 or G2 force parameters. That means that the optical potential is not only sensitive to RLF or MRW but also to the use of NL3 or G2 densities. Investigating the figure, it is clear that the extreme values of the magnitude of the real and the imaginary parts of the scalar potential are $-382.9$ and 110.6 MeV for RLF (NL3)

and −372.4 and 177.8 MeV for RLF (G2), respectively. The same values for the MRW parametrization are −217.7 and 40.2 MeV with the NL3 and −333.8 and 61.7 MeV with the G2 sets. In case of the vector potential, the extreme values for the real and imaginary parts are 293.0 and −136.0 MeV for RLF (NL3) and 319.7 and −157.5 MeV for RLF (G2), but with MRW parametrization these appear at 124.1 and −82.3 MeV with the NL3 and 115.5 and −77.1 MeV with the G2. From these variations in the magnitude of scalar and vector potentials, it is clear that the predicted results not only depend on the input target density, but they are also sensitive to the kinematics of the reaction dynamics. A further analysis of the results for the optical potential with RLF shows that the $U_{\rm opt}$ value extends for a larger distance than MRW. For example, with RLF the central part of $U_{\rm opt}$ is more expanded than MRW and ends at $r \sim 5$ fm, whereas the $U_{\rm opt}$ persists until $r \sim 6$ fm. It is important to point out that, due to the lack of availability of experimental data for the optical potential, we are unable to justify the capability of parametrizations at different energies. We also repeated the calculations without Pauli blocking and found almost identical results for the optical potential at $E_{\rm lab} \sim 300$, 800, and 1000 MeV. The effects of RLF and MRW parametrizations are presented in the next subsections during the discussion of scattering observables.

### C. Differential scattering cross section

Evaluation of the differential elastic scattering cross section $\frac{d\sigma}{d\Omega}$, defined in Eq. (40), is crucial to study the scattering phenomena. The results of our calculation for $\overrightarrow{p} + {}^{40}$Ca and $\overrightarrow{p} + {}^{40,42,44,48}$Ca systems at incident energies 300, 800, and 1000 MeV, respectively, are displayed in Figs. 5–7 along with the available experimental data [44–46]. As is stated earlier, the RIA prediction with the NL3 density is a better the choice of G2 for all the angular distributions, irrespective of the use of RLF or MRW parametrizations. Again, considering the

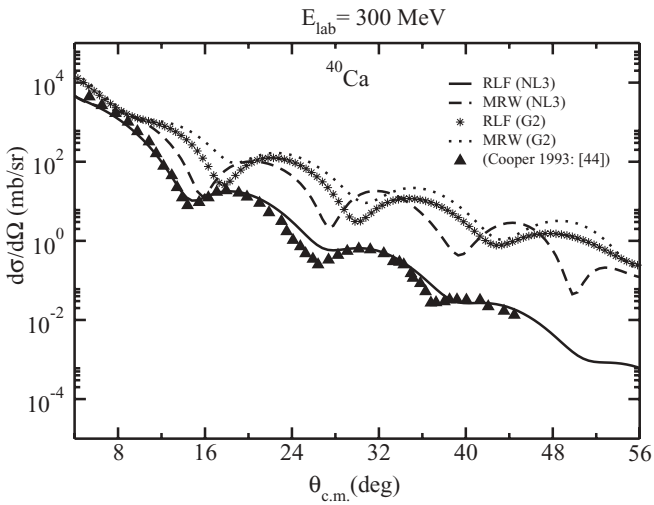


FIG. 5. The elastic differential scattering cross section ($\frac{d\sigma}{d\Omega}$) as a function of scattering angle $\theta_{\rm c.m.}$(deg) for $^{40}$Ca using both RLF and MRW parametrizations at $E_{\rm lab} = 300$ MeV. Triangles are the experimental data [44].

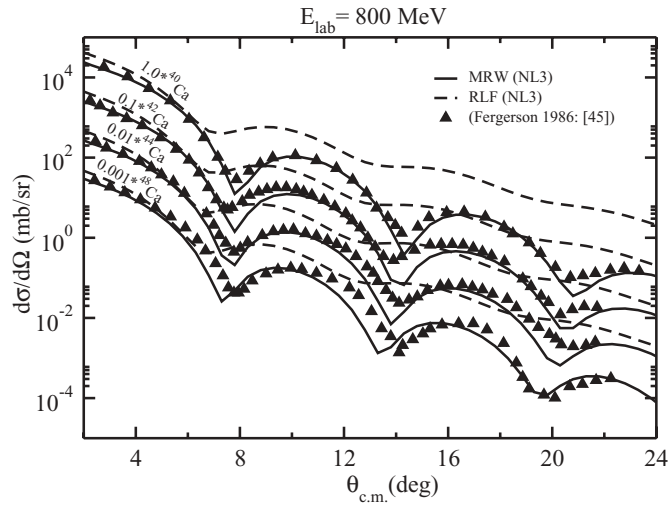


FIG. 6. Same as Fig. 5 for $^{40,42,44,48}$Ca at $E_{\rm lab} = 800$ MeV. The experimental data are taken from [45].

energy of the projectile, the RLF predictions best fit the data for $E_{\rm lab} \leqslant 400$ MeV (see Fig. 5). However, results obtained from the MRW parametrization are better for higher incident energies (Figs. 6 and 7) ($E_{\rm lab} > 400$ MeV) [19,38]. This result shows a fundamental difference between the RLF and MRW parametrization depending upon the incident energy ranges. Perhaps due to this reason, the explicit off-shell behavior of RLF and MRW drastically affects the scattering predictions. Similarly for the optical potential, the results are insensitive to the Pauli blocking.

### D. Analyzing power and spin observable

The analyzing power $A_y$ and the spin observable ($Q$ value) are calculated from the general formulas given in Eqs. (41) and (42), respectively. The results of our calculations for the $\overrightarrow{p} + {}^{40}$Ca system at incident energies 300 and 800 MeV are

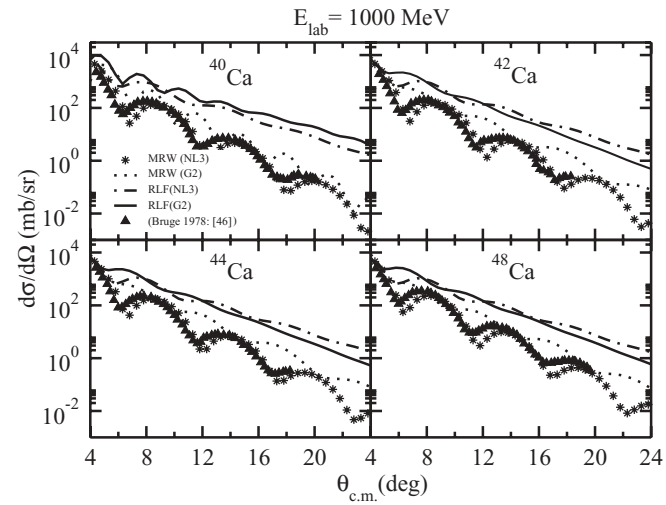


FIG. 7. Same as Fig. 6 at $E_{\rm lab} = 1000$ MeV. The experimental data are taken from [46].

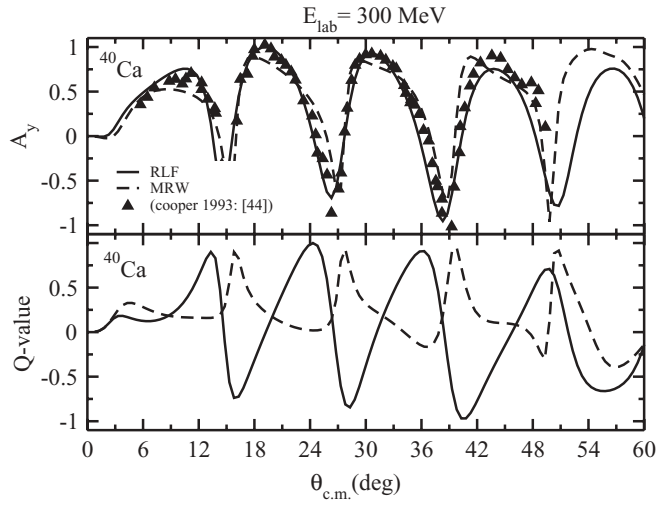


FIG. 8. Analyzing power $A_y$ and $Q$ values (spin observables) as a function of scattering angle $\theta_{\text{c.m.}}$ (deg) for $^{40}$Ca at $E_{\text{lab}} = 300$ MeV. The experimental data are taken from [44].

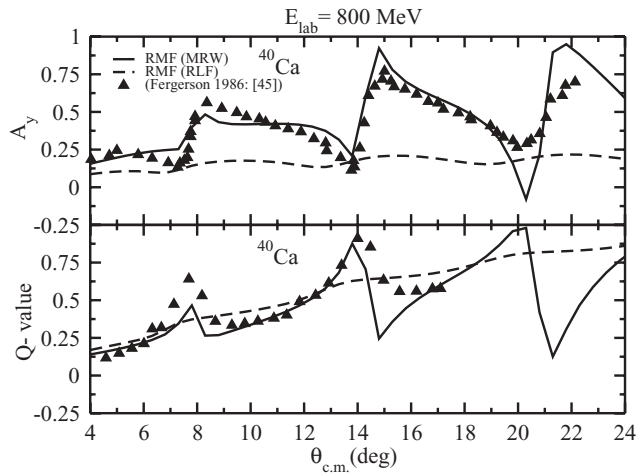


FIG. 9. Same as Fig. 8, but at $E_{\text{lab}} = 800$ MeV. The experimental data are taken from [45].

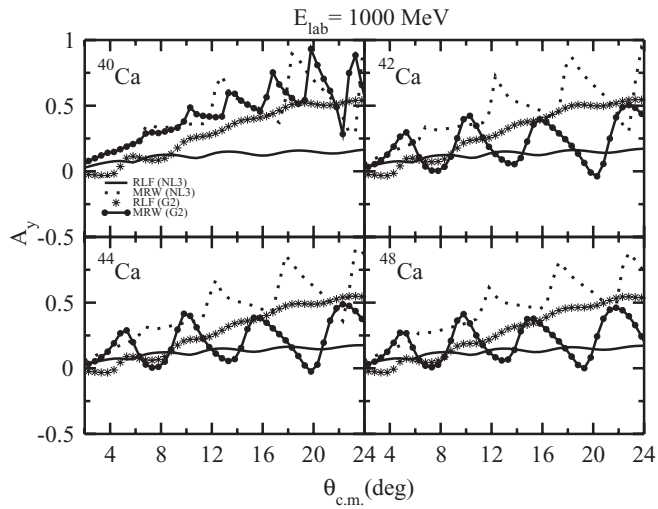


FIG. 10. Analyzing power $A_y$ as a function of scattering angle $\theta_{\text{c.m.}}$(deg) for $^{40,42,44,48}$Ca at $E_{\text{lab}} = 1000$ MeV.

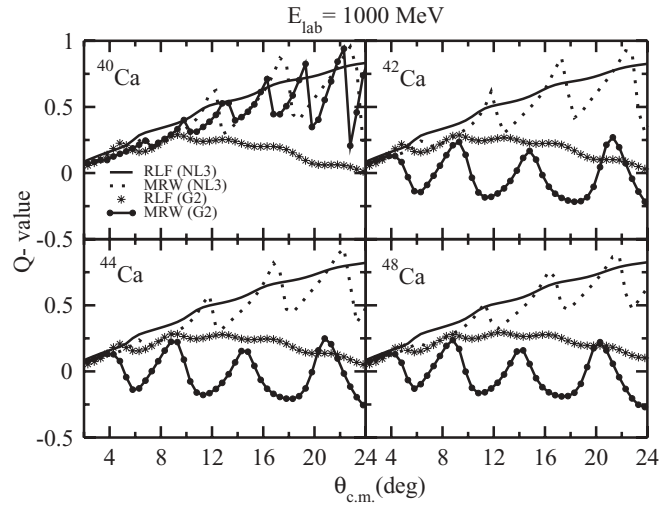


FIG. 11. The spin observable $Q$value as a function of scattering angle $\theta_{\text{c.m.}}$(deg) for $^{40,42,44,48}$Ca at $E_{\text{lab}} = 1000$ MeV.

shown in Figs. 8 and 9. The RIA predictions for $A_y$ using RLF with RMF (NL3) density show a quantitative agreement with the data [44] at 300 MeV, whereas this observation is just the reverse at 800 MeV [45]. That means that the prediction of $A_y$ resembles the $\frac{d\sigma}{d\Omega}$ observations of Figs. 5–7. In Figs. 10 and 11, we present the $A_y$ and $Q$ value for the $\overrightarrow{p} + ^{40,42,44,48}$Ca composite system at 1000 MeV. These results are obtained for both the RLF and MRW parametrizations with NL3 and G2 densities in comparision with the experimental data [46]. The calculated $A_y$ and $Q$ values obtained by these two forces differ significantly from each other for the choice of RLF and MRW parametrizations. Also, we observe small oscillations in the values of $A_y$ and $Q$ with the increase in scattering angle $\theta_{\text{c.m.}}$ for both RLF and MRW. This oscillatory behavior could be related to the dispersion phenomenon of the optical potential. Similar to the $\frac{d\sigma}{d\Omega}$, here also the prediction of MRW is best fitted to the data for the higher incident energies and RLF for lower incident energies. Further, investigation into the spin rotation parameter $Q$ value shows that the peak shift and diminished magnitude with the increase in neutron number (see Fig. 11) agree with the calculation of first-order Brueckner theory using Urbana V14 soft core internucleon interactions [47]. It makes the nucleon finite size correction more realistic and hence merits a structure effect for the formation of exotic nuclei in the laboratory.

## VI. SUMMARY AND CONCLUSION

We have calculated the density distribution of protons and neutrons for $^{40,42,44,48}$Ca by using RMF (NL3) and ERMF (G2) parameter sets. From these densities, we estimate the relative isotopic neutron density difference for both force parameters. The comparison of $\Delta\rho_n(r)$ with the data [42] indicates the superiority of G2 over NL3. The small difference in the density at the central region significantly affects the results of scattering observables including the optical potential. A fundamental difference between RLF and MRW parametrizations as well as RMF (NL3) and ERMF (G2) sets

in the RIA predictions is noticed from the observation of the $\frac{d\sigma}{d\Omega}$, $A_y$, and $Q$ values. We conclude from our calculations that RLF relatively works well at lower and MRW at higher incident energies. The predicting capability of scattering observables of RMF (NL3) over ERMF (G2) is also realized.

In conclusion, the reaction dynamics highly depends on the input density and the choice of parametrization. In addition to this, our present study indicates that the RIA is a powerful predictive model which provides a clear picture of the successful Dirac optical potentials and can be useful to study both stable and exotic nuclei.

## ACKNOWLEDGMENTS

We thank BirBikram Singh for a careful reading of the manuscript. This work is supported in part by UGC-DAE Consortium for Scientific Research, Kolkata Center, Kolkata, India (Project No. UGC-DAE CRS/KC/CRS/2009/NP06/1354).

## APPENDIX

If RLF is our choice, the $t^L$ functions in Eqs. (17)–(19) and (23), (24) involve all the occupied states for $pp$ and $pn$ scattering. It is most convenient to shift variables from $x' \rightarrow x + x'$ so the $t^L$ functions are not involved in the angular integration. Now, the first-order optical potential Eq. (20) can be written as [38]

$$U^L(r, E) = \frac{-4\pi ip}{M}\left[\int d^3r'\rho^L(x+x')t_D^L(r'; E)\right] + \left[\int d^3r'\rho^L(x+x', x)t_X^L(r'; E)j_0(pr')\right]. \tag{A1}$$

After $\phi$ integration, this becomes

$$U^L(r, E) = \frac{-8\pi^2 ip}{M}\left[\int dr' t_D^L(r'; E)\int_{-1}^{+1}\rho^L(x+x')d\omega\right] + \left[\int dr' t_X^L(r'; E)j_0(pr')\int_{-1}^{+1}\rho^L(x+x', x)d\omega\right], \tag{A2}$$

where $\omega = \cos\theta$, $(|x+x'|^2) = (r^2 + r'^2 + 2\omega rr')$, and $(\frac{|2x+x'|}{|4|}^2) = \frac{1}{4}(r'^2 + 4\omega rr' + 4r^2)$. The integral is evaluated by the Gauss-Laguerre quadrature. At the point $(x + x')$, the radial integration must go roughly twice the nuclear radius. Note that for spherical nuclei only the scalar and vector are taken into account, as the tensor terms are negligible.

In the case of MRW, the optical potential $U_{\text{opt}}$ is calculated somewhat differently from the RLF. Here we tranform the density $\rho^L(x)$ to momentum space, then multiply with the $\mathcal{F}^L(q, E)$ and back which leads to the equation

$$U^L(r, E) = \frac{-4\pi ip}{M}\left[\int \frac{d^3q}{(2\pi)^3}e^{iqx}\mathcal{F}^L(q, E)\int d^3x' e^{-iqx'}\rho^L(r')\right], \tag{A3}$$

with $\mathcal{F}^L(q, E) = \mathcal{F}_0^L(E)e^{-q^2\beta^2(E)}$ at each proton energy $E$. The final equation is obtained by adding the contributions from proton and neutron states to the direct term Eq. (A3) which is given as

$$U^L(r, E) = \frac{-8ip}{M}\frac{1}{r} \times \left[\int_0^\infty dq\sin(qr)\int_0^\infty dr'r'\sin(qr')\mathcal{F}_0^L(E)e^{-q^2\beta^2(E)}\rho^L(r')\right]. \tag{A4}$$

These integrals are solved by double Gaussian summation methods.

[1] Z. P. Li, G. C. Hillhouse, and J. Meng, Phys. Rev. C **78**, 014603 (2008).
[2] A. Amorim and F. D. Santos, Phys. Lett. B **297**, 31 (1992).
[3] B. G. Todd and J. Piekarewicz, Phys. Rev. C **67**, 044317 (2003).
[4] J. Meng, H. Toki, S. G. Zhou, S. Q. Zhang, W. H. Long, and L. S. Geng, Prog. Part. Nucl. Phys. **57**, 470 (2006).
[5] G. F. Chew, Phys. Rev. **80**, 196 (1950).
[6] V. V. Balashov and J. V. Meboniya, Nucl. Phys. A **107**, 369 (1968).
[7] R. J. Glauber, Phys. Rev. **100**, 242 (1955).
[8] L. D. Faddeev and V. A. Steklova, Akad. Nauk SSSR, Moscow **69**, 369 (1963); J. V. Meboniya and T. I. Kvarackheliya, Phys. Lett. B **90**, 17 (1980).
[9] C. Mahux, *Microscopic Optical Potentials: Proceedings of the Hamburg Topical Workshop on Nuclear Physics, University of Hamburg, September 25–27, 1978*, edited by H. V. von Geramb (Springer, New York, 1979), p. 1.
[10] H. O. Meyer, P. Schwandt, G. L. Moake, and P. P. Singh, Phys. Rev. C **23**, 616 (1981).
[11] A. D. Bacher *et al.*, IUCF Scientific and Technical Report, 1980, p. 26 (unpublished).
[12] Z. A. Khan and Minita Singh, Int. J. Mod. Phys. E **16**, 1741 (2007).
[13] D. Chauhan and Z. A. Khan, Phys. Rev. C **80**, 054601 (2009).
[14] S. Hama, B. C. Clark, E. D. Cooper, H. S. Sherif, and R. L. Mercer, Phys. Rev. C **41**, 2737 (1990).
[15] G. A. Lalazissis, J. König, and P. Ring, Phys. Rev. C **55**, 540 (1997).
[16] R. J. Furnstahl, B. D. Serot, and H. B. Tang, Nucl. Phys. A **615**, 441 (1997); R. J. Furnstahl and B. D. Serot, *ibid.* **671**, 447 (2000).
[17] C. J. Horowitz, Phys. Rev. C **31**, 1340 (1985).
[18] D. P. Murdock and C. J. Horowitz, Phys. Rev. C **35**, 1442 (1987).
[19] J. A. McNeil, L. Ray, and S. J. Wallace, Phys. Rev. C **27**, 2123 (1983).
[20] S. K. Patra and C. R. Praharaj, Phys. Rev. C **44**, 2552 (1991); Y. K. Gambhir, P. Ring, and A. Thimet, Ann. Phys. (NY) **198**, 132 (1990).
[21] M. Del Estal, M. Centelles, X. Viñas, and S. K. Patra, Phys. Rev. C **63**, 044321 (2001); S. Ohya, H. Sato, T. Izumikawa, J. Goto, S. Muto, and K. Nishimura, Phys. Rev. C **63**, 044314 (2001);

S. K. Patra, M. Del Estal, M. Centelles, and X. Viñas, *ibid.* **63**, 024311 (2001).
[22] B. D. Serot and J. D. Walecka, Int. J. Mod. Phys. E **6**, 515 (1997).
[23] R. J. Furnstahl, B. D. Serot, and H. B. Tang, Nucl. Phys. A **598**, 539 (1996).
[24] J. R. Shepard, J. A. McNeil, and S. J. Wallace, Phys. Rev. Lett. **50**, 1443 (1983).
[25] B. C. Clark, S. Hama, R. L. Mercer, L. Ray, and B. D. Serot, Phys. Rev. Lett. **50**, 1644 (1983).
[26] B. C. Clark, S. Hama, R. L. Mercer, L. Ray, G. W. Hoffmann, and B. D. Serot, Phys. Rev. C **28**, 1421 (1983).
[27] J. A. Tjon and S. J. Wallace, Phys. Rev. C **32**, 1667 (1985).
[28] D. P. Murdock, Ph.D. thesis, Massachusetts Institute of Technology, 1987.
[29] F. A. Brieva and J. R. Rook, Nucl. Phys. A **291**, 317 (1977).
[30] C. J. Horowitz and B. D. Serot, Phys. Lett. B **137**, 287 (1984).
[31] R. Brockmann and R. Machleidt, Phys. Lett. B **149**, 283 (1984).
[32] R. Machleidt and R. Brockmann, Phys. Lett. B **160**, 364 (1985).
[33] B. ter Haar and R. Malfliet, Phys. Lett. B **172**, 10 (1986); Phys. Rev. Lett. **56**, 1237 (1986).
[34] C. J. Horowitz and B. D. Serot, Nucl. Phys. A **464**, 613 (1986); Phys. Rev. Lett. **86**, 760(E) (1986).
[35] S. E. Koonin, *Computational Physics* (Benjamin, Reading, MA, 1986).
[36] W. R. Gibbs, *Computational in Modern Physics* (World Scientific, Singapore, 1994).
[37] I. E. McCarthy, *Introduction to Nuclear Theory* (Wiley, New York, 1968).
[38] C. J. Horowitz, D. P. Murdock, and B. D. Serot (Indiana University Report No. IU/NTC 90-01, 1990), (unpublished); *Computational Nuclear Physics*, edited by K. Langanke, J. A. Maruhn, and S. E. Koonin (Springer, Berlin, 1991), Vol. 1, Chap. 7, p. 129.
[39] I. Sick, J. B. Bellicard, J. M. Cavedon, B. Frous, M. Heut, P. Leconte, P. X. Ho, and S. Platchkov, Phys. Lett. B **88**, 245 (1979).
[40] L. Ray, Phys. Rev. C **19**, 1855 (1979).
[41] G. A. Lalazissis and S. E. Massen, Phys. Rev. C **55**, 2427 (1997).
[42] L. Ray, G. W. Hoffmann, M. Barlett, J. McGill, J. Amann, G. Adams, G. Pauletta, M. Gazzaly, and G. S. Blanpied, Phys. Rev. C **23**, 828 (1981).
[43] J. W. Negele and D. Vautherin, Phys. Rev. C **5**, 1472 (1972).
[44] E. D. Cooper, S. Hama, B. C. Clark, and R. L. Mercer, Phys. Rev. C **47**, 297 (1993).
[45] R. W. Fergerson *et al.*, Phys. Rev. C **33**, 239 (1986).
[46] G. Bruge, International Report D. Ph-N/ME/78-1 CEN, Salay, 1978 (unpublished).
[47] M. Hemalatha, S. Kailash, W. Haider, and Y. K. Gambhir, *Proceedings of the International Symposium on Nuclear Physics*, edited by R. K. Choudhury, A. K Mohanty, A. Saxena, K. Mahata, and S. Santra (BARC, Mumbai, 2009), Vol. 54, p. 270.